Journal of Asian Earth Sciences 259 (2024) 105919

Contents lists available at ScienceDirect

Journal of Asian Earth Sciences

journal homepage: www.elsevier.com/locate/jseaes

Tectono-thermal evolution of the northern Tarim Basin, Central Asia: New insights from apatite low-temperature thermochronometers

Jian Chang [a,b,*], Lei Yang [a,b], Chenxing Li [a,b], Nansheng Qiu [a,b], Haizu Zhang [c], Xiang Wang [c]

[a] State Key Laboratory of Petroleum Resources and Prospecting, China University of Petroleum, Beijing 102249, China
[b] College of Geosciences, China University of Petroleum, Beijing 102249, China
[c] Research Institution of Petroleum Exploration and Development, Tarim Oilfield, PetroChina, Kolar 841000, China

ARTICLE INFO

Keywords:
Kuqa fold-and-thrust belt
Central Asia
Apatite low-temperature thermochronometer
Thermal history
Hydrocarbon accumulation

ABSTRACT

The research on the tectono-thermal histories of the northern Tarim Basin, particularly the eastern Kuqa fold-and-thrust belt (KFTB) is crucial for comprehending the basin-mountain tectonic evolution and related coupling in the central Asia. This study aims to reconstruct the tectono-thermal history of the eastern KFTB with a combination of apatite fission track (AFT) ages, apatite (U-Th)/He (AHe) ages and vitrinite reflectance data. The central AFT ages of the samples range from 22.93 Ma to 156.59 Ma, which are younger than the corresponding stratigraphic ages. The single-grain AHe ages range from 4.23 Ma to 24.92 Ma and display some dispersion, likely due to radiation damage and/or grain size effects. Thermal modeling results indicate that the eastern KFTB mainly experienced the Cretaceous and Miocene rapid cooling events (althouth the timing and magnitude of these events varied among the samples), which were related to the collisions of the Qiangtang-Lhasa Terranes and India Plate with the southern margin of the Eurasia Plate. The paleo-heat flow of the eastern KFTB decreased from the Late Triassic (54 ~ 55 mW/m^2) to the Early Miocene (44 ~ 47 mW/m^2) and then increased since the Late Miocene due to thrust fault activity. Furthermore, we reappraised the maturation evolution histories of the source rock in the Huangshanjie and Yangxia formations using the new thermal hirtories, which were consistent with the hydrocarbon charging and accumulation time, as indicated by the homogenization temperature of fluid inclusions. Overall, this study provides valuable insights into the tectono-thermal histories of the eastern KFTB. It enhances our understanding of the tectonic evolution of Central Asia and holds great significance for further hydrocarbon exploration and development in the northern Tarim Basin.

1. Introduction

The tectono-thermal evolution of the sedimentary basins is associated with the lithospheric thermal structure, crustal thinning and/or thickening, sedimentological processes, geothermal field characteristics and hydrocarbon generation. It can be reconstructed by the thermal indicator and geodynamic methods (Qiu et al., 2022). The thermal indicator methods, such as vitrinite reflectance and low-temperature thermochronometers including fission track and (U-Th)/He dating, is considered to be a more reliable method for thermal history reconstruciton due to its constraints on the measured values of samples (Qiu et al., 2022). Some sedimentary basins in the world, such as Tarim, Sichuan and Bohai Bay basins in China (Qiu et al., 2022), Otway basin in Australia (Gleadow et al., 1983), Swiss Molasse Basin (Mazurek et al., 2006) and Taranaki Basin in New Zealand (Crowhurst et al., 2002), were systematacially studied by a variety of the thermal indicators. Fold-and-thrust belts in the margin of the sedimentary basins are transitional zones between orogenic belts and intracratonic basins, commonly forming at the piedmonts of active orogenic belts. The Kuqa fold-and-thrust belt in the northern Tarim Basin serves as a suitable area for studying the correlation between the Tianshan uplifting and Tarim Basin subsidence, as well as being an important region for hydrocarbon exploration (Yin et al., 1998; Wei et al., 2021; Chang et al., 2022). The discoveries of giant oil and gas fields such as Kela 2, Dina, Zhongqiu and Dabei in the Kuqa fold-and-thrust belt indicate favorable exploration prospects. Multiple unconformities observed in the Meso-Cenozoic strata suggest that the KFTB has experienced several tectonic uplifting and exhumation events (He et al., 2009), although the exact timing and extent of these events remain unknown. Previous studies have primarily focused on the Cenozoic tectonic deformation of the KFTB by analyzing

* Corresponding author at: State Key Laboratory of Petroleum Resources and Prospecting, China University of Petroleum, Beijing 102249, China.
E-mail address: changjian@cup.edu.cn (J. Chang).

https://doi.org/10.1016/j.jseaes.2023.105919
Received 26 July 2023; Received in revised form 23 October 2023; Accepted 10 November 2023
Available online 11 November 2023

the growth faults (Yin et al., 1998; Lu et al., 1999), seismic sections (Wang et al., 2011), active folds and faults (Hubert-Ferrari et al., 2007), low-temperature thermochronological data (Dumitru et al., 2001; Wang et al., 2009a; Chang et al., 2017, 2021, 2022) and magnetostratigraphic data (Huang et al., 2006, 2010; Zhang et al., 2014, 2015, 2016, 2020). However, the Meso-Cenozoic thermal histories of the KFTB have only been discussed by Yu et al. (2014) and Tang et al. (2014). Yu et al. (2014) considered that the Tuziluoke anticline in the western KFTB began deformation since ~ 5 Ma with the thermal modeling of apatite (U-Th)/He data. Tang et al. (2014) only discussed the paleo-heat flow histories of several wells in the KFTB by the vitrinite reflectance data (Ro). Moreover, the differential landforms, oil–gas phases and subsalt structural features provide evidence that the western and eastern KFTB (separated by the Kuqa River) have experienced distinct thermal histories (Wang et al., 2011; Wei et al., 2021 Xu et al., 2020).

Each thermal indicator usually only records the thermal information of the sedimentary basins at a specific period. Vitrinite reflectance data can record the maximum temperature experienced by the sedimentary formations, while the low-temperature thermochronometers can provide information about the specific temperature range encountered by the strata, i.e., apatite fission track ages can record the thermal histories within the temperature rangte of 60 ~ 120 ℃. By combining multiple thermal indicators, such as joint inversion with vitrinite reflectance and low-temperature thermochronometer data, we can gain a more accurate understanding of the thermal history of sedimentary basins. However, previous studies on the thermal histories of the KFTB only utilized a single thermal indicator (Yu et al., 2014; Tang et al., 2014), which may lead to missing of some important thermal information. Compared with the eastern KFTB, the western KFTB received thick Cenozoic sediments, which caused that the thermal indicators only record the present-day thermal information. Therefore, the thermal indicators were not suitable for studying the tectono-thermal evolution of the western KFTB.

In this study, we aim to reconstruct the tectono-thermal history of the eastern KFTB by using the new vitrinite reflectance, apatite fission track, and (U-Th)/He data of both outcrop and drilling samples. Firstly, the stages, time, and amplitude of the uplift events in the eastern KFTB were revealed using joint inversion of AFT and AHe data. Secondly, we modeled the heat flow history of the KFTB based on the burial histories and Ro data. Finally, we discuss the possible triggers for these tectonic uplift events and their implications for hydrocarbon migration and

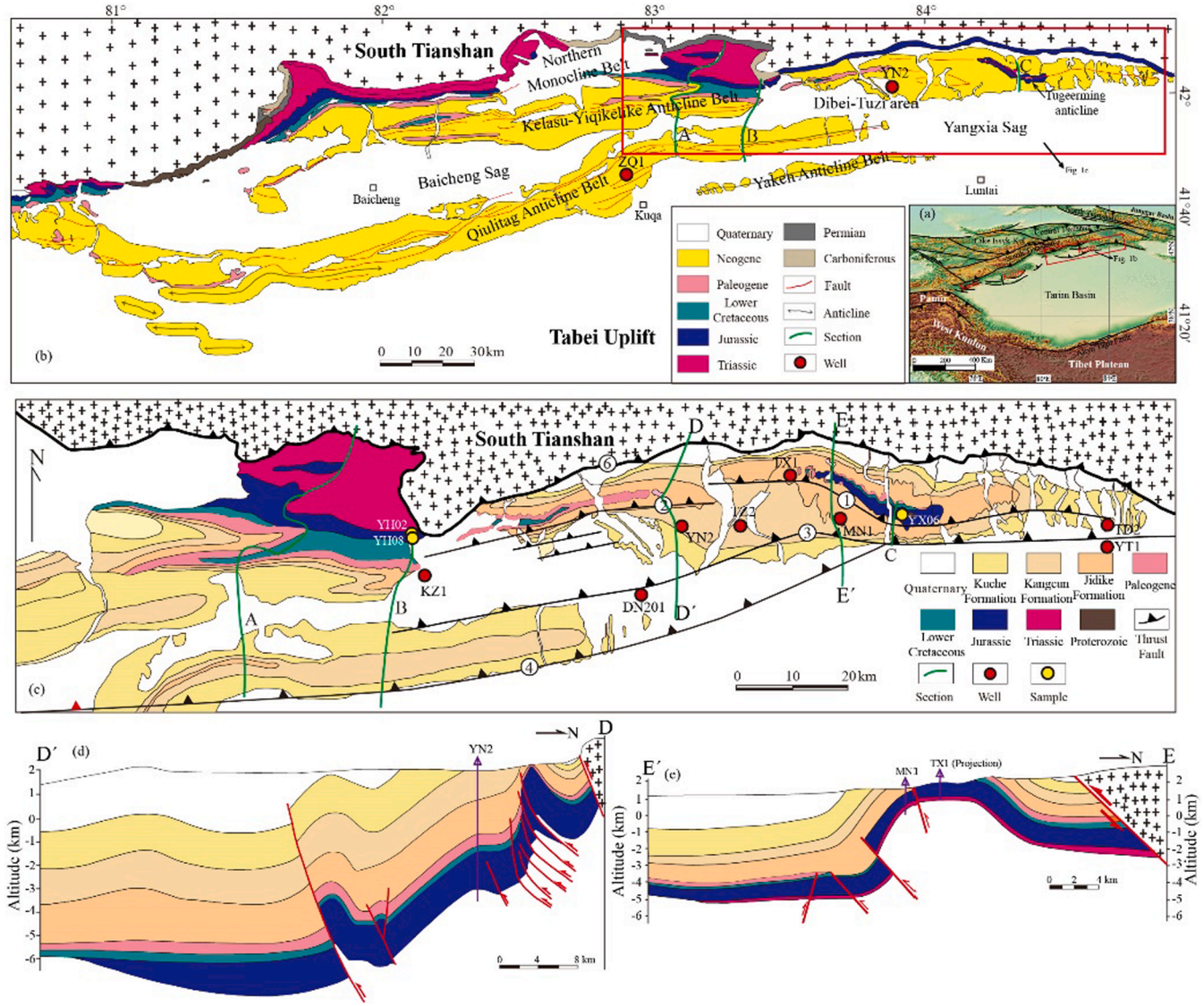

Fig. 1. (a) Geomorphologic map of the Central Asia with some primary faults, showing the location of Kuqa fold-and-thrust belt; (b) Geological map of the KFTB showing five secondary structural units; A-Kuqa River Section; B-Yaha Section; C-Yangxia Section; (c) Geological map of the eastern KFTB showing the main faults and studied wells (Modified from Wei et al., 2016). ①-Tugeerming Fault; ②-Yiqikelike Fault; ③-Tuziluoke Fault; ④-East Qiulitag Fault. (d&e) The DD′ and EE′cross sections. Their locations were shown in Fig. 1c.

accumulation. This study provides new insights into the tectono-thermal histories and hydrocarbon maturation evolution in the eastern KFTB, which will be of great significance for future hydrocarbon exploration and tectonic evolution in this region.

2. Geological setting

The KFTB, located in the northern Tarim Basin, is bounded by the South Tianshan to the north and the Tabei Uplift (a secondary tectonic unit of the Tarim Basin) to the south. It can be divided into five secondary structural units from north to south: the Northern Monocline Belt, the Kelasu-Yiqikelike Thrust Belt, the Baicheng sag, the Yangxia sag and the Qiulitag Anticline Belt (Fig. 1b). The eastern KFTB (east of the Kuqa River) consists of the eastern Kelasu-Yiqikelike Thrust Belt, Yangxia sag and eastern Qiulitag Anticline Belt (Fig. 1c). In addition, several major thrust faults, such as the Tugeerming Fault, Yiqikelike Fault, Tuziluoke Fault, and eastern Qiulitag Fault, can be observed in the eastern KFTB (Fig. 1c).

The KFTB developed on the Paleozoic fold basement and experienced three evolutionary stages, which includes the Late Permian-Triassic foreland basin, the Jurassic-Paleogene extensional depression basin and the Neogene-Quaternary rejuvenated foreland basin (He et al., 2004, 2009; Fig. 2). The KFTB developed from the Early Triassic fluvial and alluvial facies to the Late Triassic lacustrine and delta facies and deposited massive sandstone, mudstone, and conglomerate with several sets of coal layers in the Tajike Formation. In the Early Jurassic, the configuration of the KFTB was characterized by a northward-dipping slope, accompanied by a shift in tectonic stress from compression to extension. The KFTB then developed with braided-fluvial facies and lacustrine-swamp facies. The Yangxia Formation, for example, exhibits clastic rocks with the thickness of 500 ~ 2200 m (Fig. 1b and 1c). During the Late Jurassic-Early Cenozoic, most of Central Asia developed a paleo-planation surface and experienced slow uplifting and exhumation (Morin et al., 2019; Jolivet, 2015). The northern KFTB was characterized by the alluvial fan and alluvial plain from the Late Jurassic to Early Cretaceous. A parallel unconformity between the conglomerates of the Lower Cretaceous Yageliemu Formation and the maroon sandy conglomerates of the Upper Jurassic Kalaza Formation suggests a proximal and rapid deposition process. The Lower Cretaceous Shushanhe Formation in the KFTB primarily consists of siltstones and mudstones with thicknesses ranging from 40 to 1100 m. The absence of Upper Cretaceous deposits suggests that the entire KFTB likely experienced a paleo-

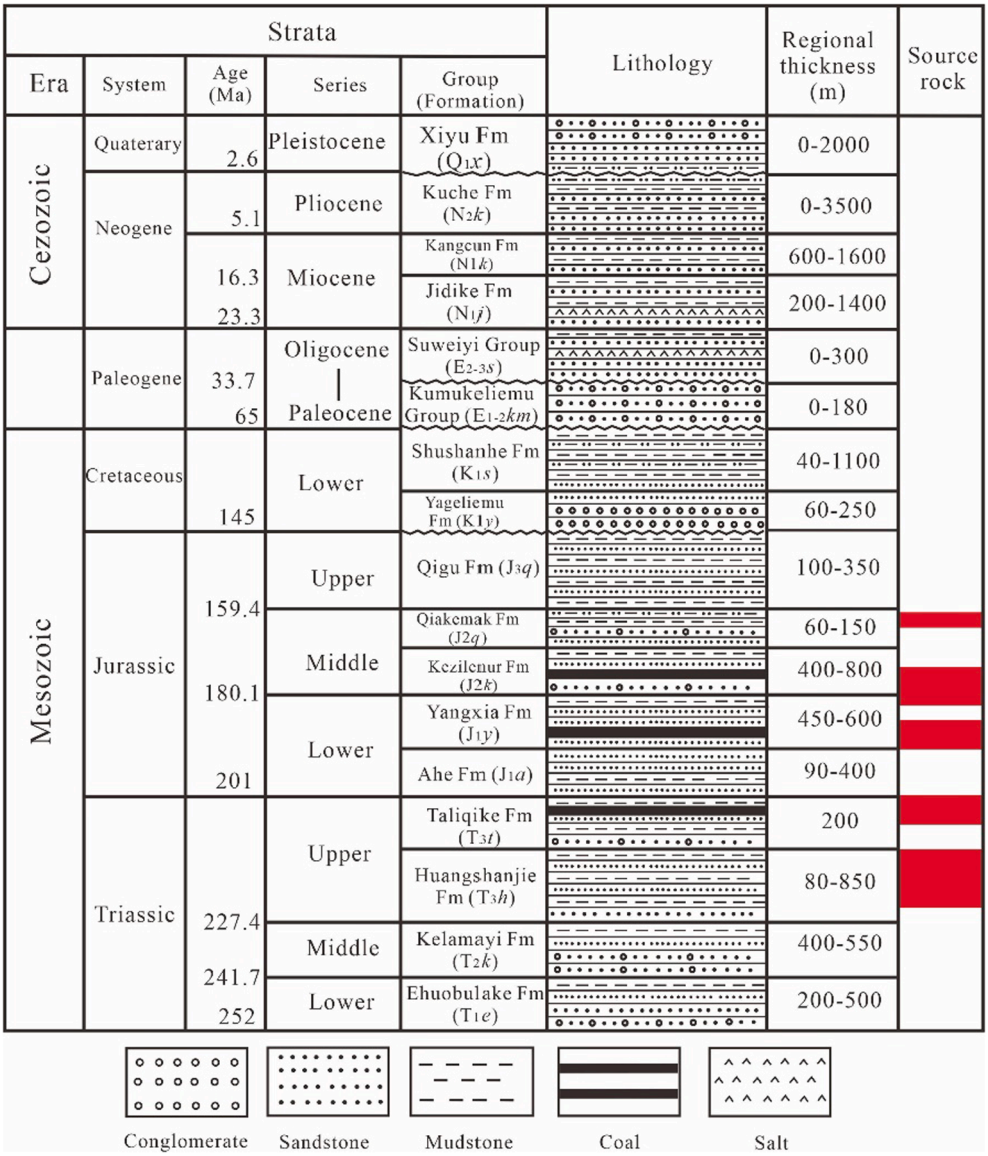

Fig. 2. Generalized stratigraphic column of the Kuqa fold-and-thrust belt (Modified from Chang et al., 2019).

planation stage during the Late Cretaceous with gradual exhumation (Chang et al., 2022). During the Kumugeliemu period, the western KFTB deposited the thick gypsum-salt rock and mudstones due to the transgression of the Neo-Tethys Ocean, while the eastern KFTB continued to undergo exhumation. In the Neogene, the KFTB transformed into a rejuvenated foreland basin with the far field effect of the collision between India and Eurasia plates and deposited the clastic sediments with thicknesses of up to 2000 m.

The Upper Triassic and Jurassic lacustrine mudstone, coal shales, and coal beds present in the KFTB are considered to be good source rocks, while the Mesozoic sandstone and conglomerate layers often serve as reservoirs (Fig. 2). The gypsum-salt rocks found in the Kumugeliemu Group and Jidike Formation not only act as cap rocks for oil and gas reservoirs but also serve as important detachment layers. These gymsum-salt rocks play a significant role in controlling thrust deformation within the KFTB, as evidenced by field investigation, seismic data, and structural physical simulations (Tang et al., 2004, 2006; Wang et al., 2009b; Li et al., 2012).

3. Sampling strategy and experiment methods

In this study, we collected seven samples YH-02, YH-08, YH-15, YX-06, TX1-03, YN2-07 and MN1-04 to investigate the tectono-thermal histories of the eastern KFTB based on the measured apatite fission track (AFT) and apatite (U-Th)/He (AHe) data (Table 1, 3 and 4). The AFT and AHe data are sensitive to the temperature ranges between 40 ℃ and 120 ℃, making them suitable to study cooling histories under low-temperature conditions. In addition, vitrinite reflectance data from the Tarim Oilfield of the CNPC were used to determine the maximum temperatures experienced by the samples and reconstruct the paleo-heat flow histories of the eastern KFTB by employing the Easy% Ro model (Sweeney and Burnham,1990; Table 5).

The AFT analysis was carried out at the thermochronology laboratory of China University of Petroleum, Beijing. The apatite grains were first mounted in epoxy resin for 48 h, then ground to expose their maximum internal surfaces, and finally polished to remove surface fractures. The mounts were etched in 5.5 M HNO_3 for 20.0 ± 0.5 s at 21 ± 1 °C to reveal the spontaneous fission tracks intersecting the polished apatite grain surfaces. The spontaneous tracks were manually counted on digital images using both reflected and transmitted light at a magnification of 1000× on a Zeiss Image.M2m microscope operating under Autoscan Trackworks control software. For each sample, only grains with polished surfaces parallel to the c-crystallographic axis were selected for analysis. Additionally, the horizontal confined track lengths and etch pit diameters (D_{par}) were measured using the same magnification as the track counting. All the grains with counting the spontaneous tracks were measured using an ESI NWR193nm Excimer laser coupled to a quadrupole Agilent 7900 ICP-MS for getting the U concentration. The U concentration and U/Ca ratio were calculated using Iolite 4 software. Detailed analytical conditions and measured apatite fission track data were shown in Table 2 and 3, respectively. The AFT ages were then calculated based on the spontaneous tracks and U concentration with the equation of Cogné et al. (2020). The zeta fractionation factor (ζ_{ICP}) was determined to be 0.658 ± 0.081. Subsequently, radial plots of the AFT ages were generated by the IsoplotR software (Vermeesch, 2018).

The AHe analysis involved several steps, including grain selection, helium extraction, and U-Th content measurement. The initial two steps were conducted at the thermochronology laboratory of China University of Petroleum, Beijing. Apatite grains were examined under polarized light to detect possible mineral inclusions. Only clear and euhedral grains were chosen for the AHe analysis. For each sample, Two to three apatite grains were wrapped in the 1 mm × 1 mm platinum capsules and then loaded into a 25-hole sample disc for helium extraction by the Alphachron MKII He Extraction instrument. Each grain was heated and outgassed under vacuum at ~1000 °C for 5 min using a diode laser with a wavelength of 970 nm. The extracted gas is then spiked with ^{3}He and measured by isotope dilution using a PFEIFFER quadrupole mass spectrometer. Following helium extraction, the grains were retrieved and dissolved in acid for uranium (U) and thorium (Th) measurements at the ^{40}Ar/^{39}Ar and (U-Th)/He geochronology laboratory of IGGCAS. The apatite grains were spiked and dissolved in concentrated HNO_3, and a 350 μl solution was prepared for subsequent U-Th analysis, as described by Wu et al. (2016). The dissolved samples were measured with a Thermo Fisher X-Series II inductively coupled plasma mass spectrometer (ICP-MS). The helium ages were calculated using the java-based program helioplot (Vermeesch, 2010) and corrected for α-emission following the approach of Farley et al. (1996). Replicate analyses were carried out for each sample, and detailed analysis results are listed in Table 4.

Table 1
Information of the samples reported in this study.

Sample no.	Location/Well name	Altitude/ Depth (m)	Formation	Lithology
YH-02	N42°7′45.6″ E83°24′48.3″ (Yaha Section)	2042	Middle Jurassic	Fine sandstone
YH-08	N42°7′36.6″ E83°24′49.9″ (Yaha Section)	2111	Middle Jurassic	Middle sandstone
YH-15	N42°5′1.6″ E83°23′15.3″ (Yaha Section)	1852	Lower Cretaceous	Siltstone
YX-06	N42°7′17.5″ E84°26′13″ (Yangxia Section)	1450	Middle Jurassic	Middle sandstone
TX1-03	TX1	1195	Lower Jurassic	Middle sandstone
YN2-07	YN2	4071	Middle Jurassic	Fine sandstone
MN1-04	MN1	1057	Lower Jurassic	Fine sandstone

4. Results and thermal modeling

4.1. Results

According to Table 3 and 4, the samples collected from the eastern KFTB exhibit varying AFT and AHe ages, all of which are younger than their corresponding stratigraphic ages. These ages provide insights into the thermal events experienced in the KFTB. The sample YX-06 from the Yangxia Section displays an AFT central age of 157.51 ± 29.35 Ma. Meanwhile, some single-grain AFT ages of the sample YX-06 were even older than the stratigraphic age (Fig. 3c), indicating that it just

Table 2
LA-ICP-MS analytical parameters for the apatite U concentration measurement.

Laser ablation System:	
Model	Coherent ExciStar Excimer
Ablation cell	2- vol sample cell
Wavelength	193 nm
Repetition rate	5 Hz
Fluence	2.0 J/cm^2
Ablation duration	45 s
Spot diameter	20 μm
Sampling mode	Static spot ablation
Carrier gas	100% He in the cell, N^2 added downstream
ICP-MS Instrument:	
Model	Agilent 7900
Sample introduction	Ablation aerosol
RF power	1550 W
Plasma gas flow	15 L/min
Auxilary gas flow	0.6–0.8 L/min
Massese measured	43Ca; 204Pb; 206Pb; 207Pb; 208Pb, 232Th, 238U

Table 3
Measured apatite fission track data of the samples from the eastern KFTB.

Sample No.	Depositional age (Ma)	No. grains	$\rho_s(10^5/cm^2)$ (Ns[a])	U/Ca	U(ppm)[b]	P(χ^2)[c]	Central age ± 1σ (Ma)	Mean track length ± 2σ (μm) (n[d])	Dpar (μm)
YH-08	195–190 Ma	11	4.755(84)	0.0175347	71.73879016	0.19	22.93 ± 5.85	9.87(1)	1.98(1.61 ~ 2.51)
YH-02	195–201 Ma	13	5.581(115)	0.0132483	65.50654981	0.11	31.65 ± 7.47	12.23 ± 3.19(3)	2.05(1.46 ~ 2.56)
YX-06	180–175 Ma	50	13.443(2124)	0.0076849	26.44376415	0.92	156.59 ± 7.34	10.51 ± 1.42(80)	2.10(1.52 ~ 2.92)
MN1-04	190–195 Ma	20	15.999(1308)	0.0097446	48.11891792	0.19	127.36 ± 10.64	9.43 ± 1.45(70)	2.28(1.51 ~ 3.21)
TX1-03	190–195 Ma	12	18.516(432)	0.012152	50.51502484	0.86	122.41 ± 12.12	9.63 ± 1.60(18)	1.96(1.53 ~ 2.70)
YN2-07	170–175 Ma	7	16.031(211)	0.0216907	78.39128874	0.4	66.55 ± 9.31	10.42 ± 1.61(6)	1.79(1.50 ~ 2.52)

[a] Ns: sum of spontaneous fission tracks for one sample;
[b] U (ppm): U content value gotten from the LA-ICP-MS measurement;
[c] P(χ^2): chi-square probability (Galbraith, 1981).
[d] n: number of the confined fission tracks.

Table 4
Measured apatite (U-Th)/He data of the samples from the eastern KFTB.

Sample	Grain No.	^{4}He (ncc)	Mass (μg)	U (ppm)	Th (ppm)	[eU][a] (ppm)	L[b] (μm)	W[b] (μm)	Rs[c] (μm)	T[d]	Raw age (Ma)	F_T[e]	Corrected Age ± 1σ (Ma)	Weighted Mean age[f] (Ma ± 2σ)
TX1-03	1	0.220	3.482	32.089	183.857	75.295	190.5	96	54.42	1	6.925	0.74	9.40 ± 0.09	8.88 ± 0.08
	2	0.140	2.757	23.333	185.517	66.93	168	95	53.03	1	6.24	0.73	8.55 ± 0.25	
	3	0.071	11.955	2.554	24.431	8.29	269.5	149	86.41	0	5.94	0.83	7.16 ± 0.17	
MN1-04	1	0.146	7.247	4.575	15.995	8.333	206.5	136.5	74.44	1	20.01	0.80	24.92 ± 0.33	24.95 ± 0.31
	2	0.749	14.087	15.325	23.61	20.873	275	161.5	89.67	1	21.03	0.84	25.18 ± 0.90	
YH-02	1	0.238	15.118	18.16	54.82	31.04	303.5	160	93.25	0	4.19	0.84	4.98 ± 0.07	4.92 ± 0.05
	2	0.127	7.165	27.66	35.00	35.89	182	147	81.25	0	4.08	0.82	4.98 ± 0.09	
	3	0.029	1.95	18.41	101.20	42.19	154	81	45.67	1	2.92	0.69	4.23 ± 0.19	
YH-15	1	0.021	36.336	0.53	1.29	0.83	319.5	247.5	137.64	0	5.69	0.89	6.39 ± 0.43	6.54 ± 0.33
	2	0.053	27.551	1.54	6.40	3.04	323	208.5	118.79	0	5.21	0.87	5.96 ± 0.69	
	3	0.019	26.463	0.07	3.49	0.89	315	220.5	124.34	0	6.68	0.88	7.60 ± 0.73	
YX-06	1	0.026	49.611	0.02	0.94	0.24	374	267.5	143.98	1	17.48	0.90	19.52 ± 1.15	13.37 ± 0.16
	2	0.055	41.039	0.90	1.94	1.36	366.5	249	124.94	2	8.11	0.88	9.22 ± 0.23	
	3	0.782	82.961	3.81	5.14	5.02	414.5	342.5	179.58	1	15.52	0.92	16.95 ± 0.22	

[a] Effective uranium content, [eU] = [U] + 0.235*[Th] (Shuster et al., 2006).
[b] L and W are length and width of crystal or crystal fragment, respectively.
[c] Radius of a sphere with the equivalent surface area-to-volume ratio as cylindrical crystals [Meesters and Dunai, 2002], Rs=(3*(RL))/(2*(R + L)) where R = W/2.
[d] T is Number of terminations identified on crystal, 0 = no crystal terminations, 1 T = one crystal termination and 2 T = 2 crystal terminations.
[e] F_T is the a-ejection correction after Farley et al. (1996).
[f] Weighted mean age with 95% confidence is calculated in the website https://www.isoplotr.com/isoplotr/.

Table 5
The vitrinite reflectance data of the typical wells in the eastern KFTB.

Well No.	Depth (m)	Form.	Ro (%)	Well No.	Depth (m)	Form.	Ro (%)
YT1	7044	J2	1.05	YN2	4178.5	J2	0.8
	7146	J2	0.99		4179.5	J2	0.8
	7230	J2	1.17		4250.2	J2	0.9
	7352	J1	1.08		4250.3	J2	0.85
	7465	J1	1.05		4250.37	J2	0.9
	7606	J1	0.98		4310.23	J2	0.9
	7709.6	J1	1.01		4312.83	J2	0.86
	7791.2	J1	1.08		4314.9	J2	0.86
	7802	J1	1.13		4316.6	J2	0.84
	7895	J1	1.25		4317.8	J2	1.08
	7905	T3	1.13		4318.8	J2	0.86
	7938	T3	1.13		4319.5	J2	0.83
MN1	420.09	J2	0.46		4400.5	J1	0.97
	608.59	J1	0.50		4402.8	J1	0.97
	957.4	J1	0.61		4403.7	J1	0.89
	1148.07	J1	0.64		4404.4	J1	1.11
TD2	3979.95	J1	1.16		4404.46	J1	0.81
	4139.2	J1	1.37		4405.5	J1	1.0
	4139.5	J1	1.33		4560.7	J1	1.14
TX1	1636.2	J1	0.73		4702.95	J1	0.9
YN2	3945.6	J2	0.78		5244.1	T3	1.23
	4123.93	J2	0.77		5244.3	T3	1.4
	4124.2	J2	0.81		5310.8	T3	1.43
	4124.9	J2	0.78				

experienced partial annealing after deposition in the eastern KFTB. The Jurassic samples MN1-04 and TX1-03 from wells MN1 and TX1 show AFT central ages of 127.36 ± 10.64 Ma and 122.41 ± 12.12 Ma, respectively. The Jurassic sample YN2-07, obtained from the Well YN2 at a depth of 4071.0 m, exhibits an AFT central age of 66.55 ± 9.31 Ma, slightly younger than the ages of samples MN1-04 and TX1-03. It is speculated that the current high burial temperature still keeps the sample YN2-07 annealing. The Middle Jurassic samples YH-02 and YH-08 from the Yaha Section show AFT central ages of 22.93 ± 5.85 Ma and 31.65 ± 7.47 Ma, respectively. Furthermore, these two AFT ages gradually increase from north to south in the eastern KFTB, suggesting that the northern margin of the KFTB deformed gradually from the piedmont of the Southern Tianshan to the interior of the Kuqa KFTB, which has been discussed by numerous previous studies (Chang et al., 2017, 2019, 2021, 2022; Hubert-Ferrari et al., 2007; Wang et al., 2011).

The sample YX-06 yielded three single-grain AHe ages of 19.52 ± 1.15 Ma, 9.22 ± 0.23 Ma and 16.95 ± 0.22 Ma, showing a positive correlation with the Rs (Fig. 4a). The single-grain AHe ages of the samples YH-02 and YH-15 are relatively concentrated with the range of 4.23 ~ 4.98 Ma and 5.96 ~ 7.60 Ma, showing a slightly positive correlation with the Rs and a slightly negative correlation with the eU (Fig. 4). Their weighted mean ages are 4.92 ± 0.05 Ma and 6.54 ± 0.33 Ma, indicating a late Miocene cooling event. The sample MN1-04 yielded two AHe ages of 24.92 ± 0.33 Ma and 25.18 ± 0.90 Ma with a weighted mean age of 24.95 ± 0.31 Ma, recording the Late Oligocene cooling event. The three single-grain AHe ages of the sample TX1-03 are 9.40 ± 0.09 Ma, 8.55 ± 0.25 Ma, and 7.16 ± 0.17 Ma, which show a

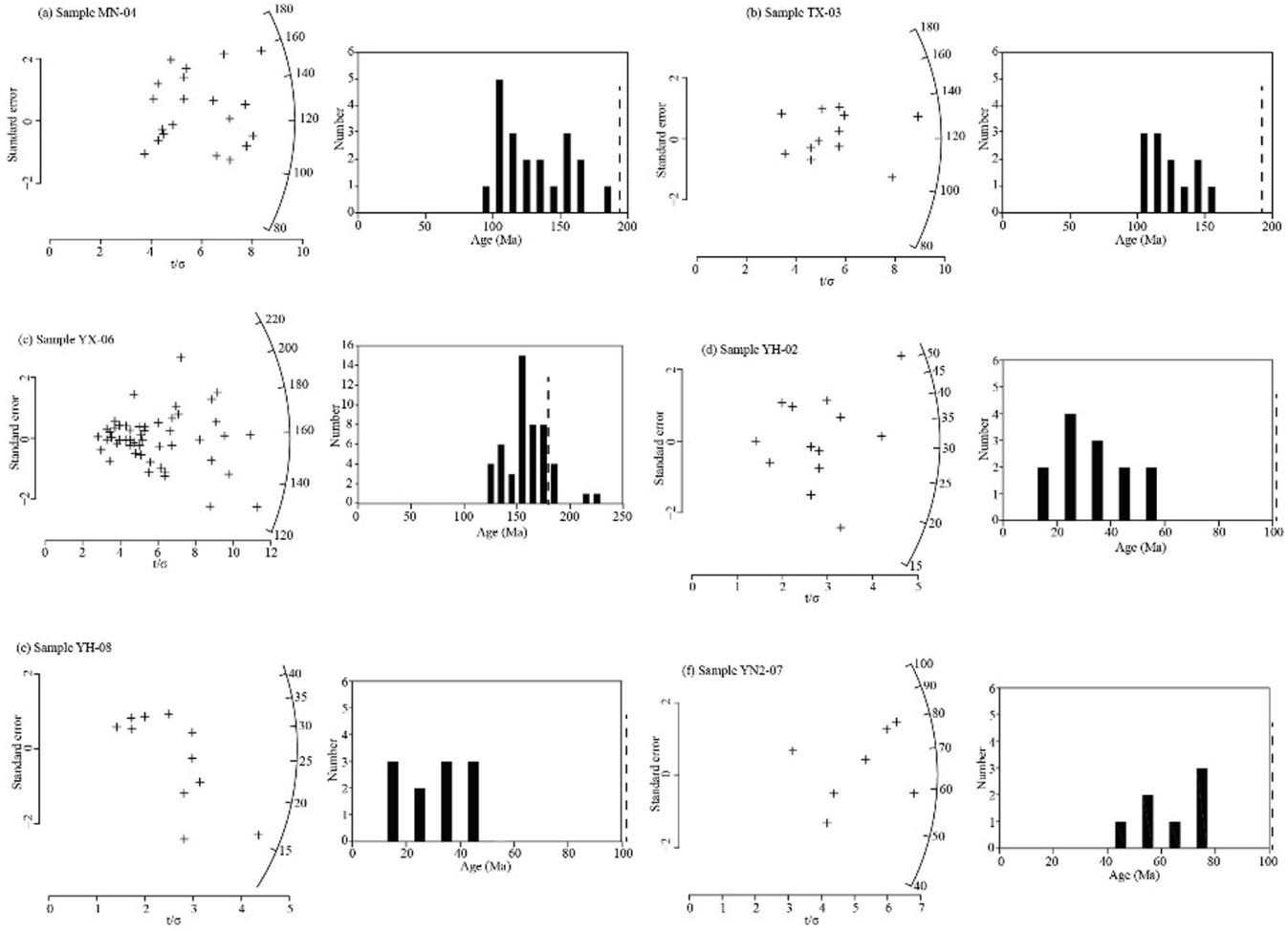

Fig. 3. Radial plots and age spectra of the measured AFT samples in the eastern KFTB. The dash line in each spectrum represents the stratigraphic age of the sample. Except for the sample YX-06, all the single-grain AFT ages of other samples are younger than the stratigraphic ages.

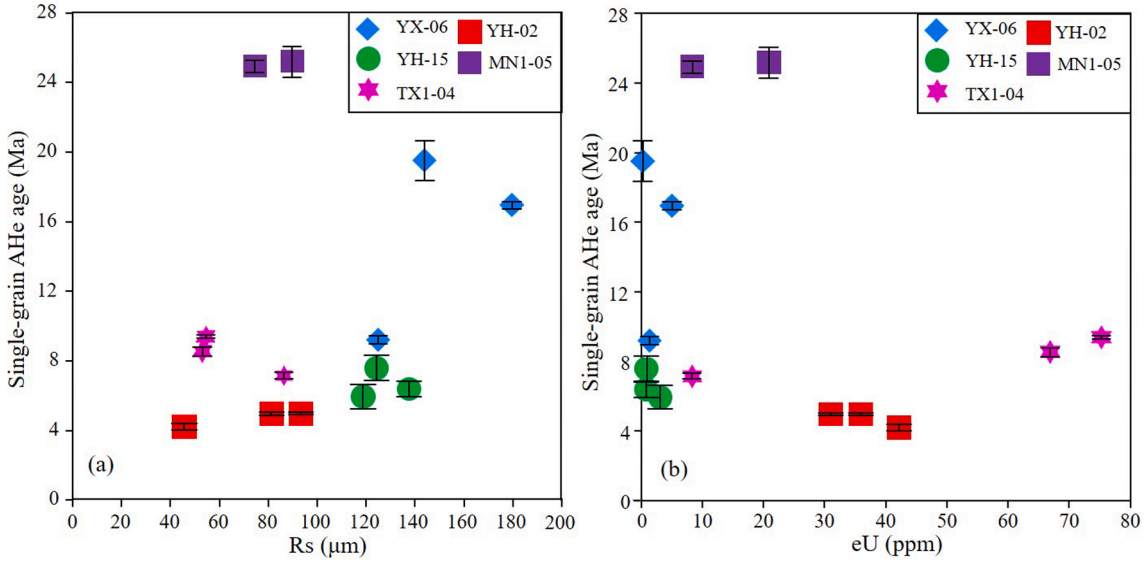

Fig. 4. Correlation of the single-grain AHe age with Rs (a) and eU (b) for the samples from the eastern KFTB.

positive correlation with eU and a negative correlation with Rs (Fig. 4). Its weighted mean age is 8.88 ± 0.08 Ma, indicating a late Miocene cooling event.

4.2. *Thermal modeling histories*

In this study, the time–temperature histories of the samples MN1-04,

TX1-03, YH-02, YH-08, and YX-06 were modeled for better understanding the thermal history of the eastern KFTB. Due to the fewer apatite grains (7) and confined tracks (6), AFT data of the sample YN2-07 are not suitable for thermal history simulation. Compared to the samples YH-02 and YH-08, the measured AHe data of the sample YH-15 only recorded the Late Miocene cooling event, and its thermal modeling cannot effectively constrain the earlier thermal information. This modeling was implemented by the HeFTy software (Ketcham, 2005). For the samples MN1-04, TX1-03, YH-02 and YX-06, the AFT and AHe data were integrated for thermal simulation, while only AFT data were used for thermal modeling of the sample YH-08. The AFT central ages and track length data were modeled using the multi-kinetic annealing model by Ketcham et al. (2007) with the measured kinetic parameter Dpar. The apatite radiation damage accumulation and annealing model developed by Flowers et al. (2009) was adopted for the measured AHe ages. In our modeling approach, the initial modeling time was set as the time when each sample was deposited in the eastern KFTB (Table 3). Both the initial and present-day surface temperature were set to be ~14 °C. For the drilling samples, the present-day temperature was calculated based on the present-day surface temperature, the present-

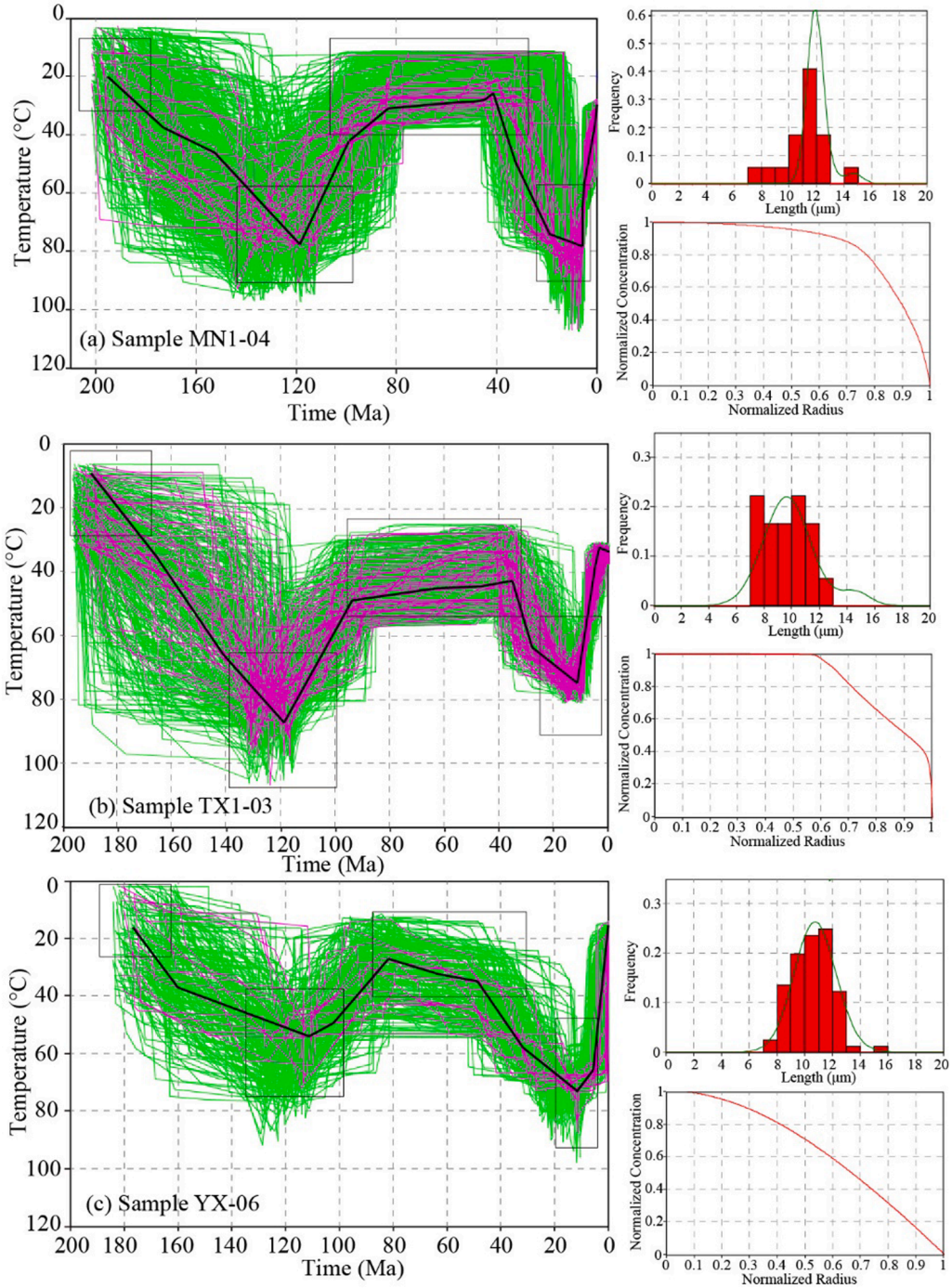

Fig. 5. Thermal histories of the samples MN1-04, TX1-03 and YX-06 using the AFT and AHe data. The left figures show the attempted temperature paths. Green lines are acceptable, magenta lines are good, and the thick black line is the best modeled thermal history. The right histograms indicate the measured and modeled AFT length distribution; the right cure graphs indicate a progression of the He concentrations from the core to the rim in a single grain (Ketcham, 2016). (For interpretation of the references to colour in this figure legend, the reader is referred to the web version of this article.)

day geothermal gradient provided by Wang et al. (2003), and the burial depth of each sample (Table 1). In addition, some additional constraints were required for the thermal modeling. According to the missing Upper Jurassic, Cretaceous and Cenozoic strata shown by the drilling data, regional tectonic evolution characteristics and measured AFT and AHe data, three constraints were chosen around the Early Cretaceous, Late Cretaceous-Eocene and Late Miocene to Quaternary time intervals for the samples TX1-03 and MN1-04. Because the outcrop sample YX-06 were located near the wells TX1 and MN1, it was assigned the same constraints. According to the distribution characteristics of residual strata in the Kuqa River and Yaha sections, three additional constraints were chosen around the Early Cretaceous-Late Cretaceous(120–80 Ma), Late Cretaceous-Paleogene (70–40 Ma) and since the Miocene for the outcrop samples YH-02 and YH-08. In our model, 100,000 thermal paths were run using a Monte Carlo inverse modeling method, with the best temperature path indicating the thermal history of the sample. It is worth noting that changes in the paleotemperature of the samples could occur due to sedimentation, uplift, or erosion events.

The thermal modeling results revealed that the samples MN1-04, TX1-03 and YX-06 experienced similar time–temperature histories, regardless of the amplitude of the cooling events (Fig. 5). The Wells MN1 and TX1 and Yangxia Section areas experienced prolonged deposition from the Early Jurassic to early Cretaceous, leading to a gradual increase in burial temperature of the samples MN1-04, TX1-03 and YX-06. Firstly, thest areas experienced a rapid cooling event at ~ 120 Ma-~80 Ma (Early Cretaceous- Late Cretaceous), which was followed by a prolonged period of slow cooling (~80 Ma-~40 Ma). Subsequently, there was a notable rapid burial and heating event from the Late Eocene to Miocene due to the burial of the geological layers. Another phase of rapid cooling began around 10 Ma and has continued since then. However, it is worth noting that the sample TX1-03 experienced subsequent heating due to deposition in the Quaternary.

The thermal modeling results of the samples YH-02 and YH-08 indicated that the Yaha Section area experienced two heating events and two cooling events (Fig. 6). During the Late Cretaceous to Early Paleogene period (100–60 Ma), both samples experienced the initial phase of rapid cooling. However, the timing of the second cooling events differs between these two samples. Sample YH-02 suggests that the Yaha Section underwent deformation and started to experience exhumation around 5 Ma. On the other hand, sample YH-08 indicated that the area began exhumation around 20 Ma, as indicated by the measured AHe ages.

5. Heat flow evolution

In this study, we collected 47 vitrinite reflectance data from wells TX1, MN1, YN2, TD2 and YT1 in the eastern KFTB (Table 5), which range from 0.46% to 1.43% and show a positive correlation with the depths (Fig. 7). In this study, the Basinmod 1D software was utilized to model the heat flow histories in the eastern KFTB by employing the Easy %Ro model developed by Sweeney and Burnham (1990). First, we rebuilt the sedimentary and burial histories of the drillings according to the borehole data, and then the constraints such as the vitrinite reflectance data and the present-day heat flow were input. Secondly, we

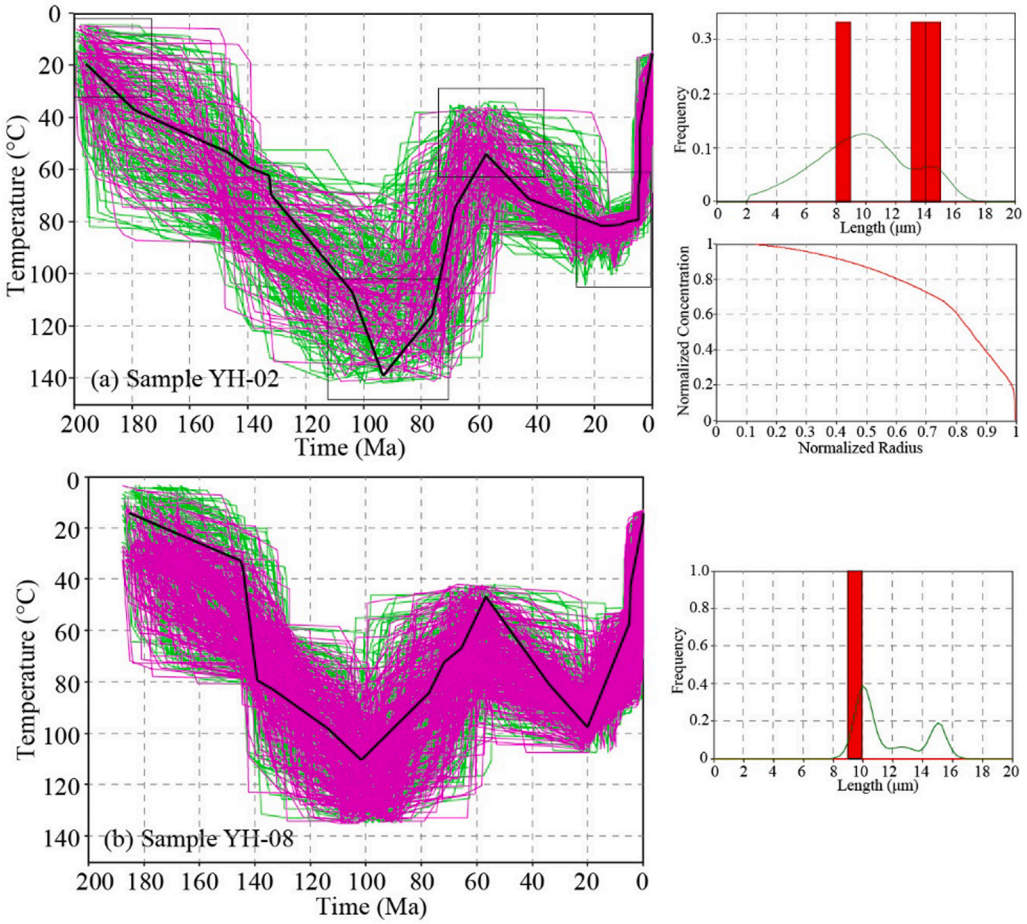

Fig. 6. Thermal histories of the samples YH-02 and YH-08. The left figures show the attempted temperature paths. Green lines are acceptable, magenta lines are good, and the thick black line is the best modeled thermal history. The right histograms indicate the measured and modeled AFT length distribution; the right cure graph indicates a progression of the He concentrations from the core to the rim in a single grain (Ketcham, 2016). (For interpretation of the references to colour in this figure legend, the reader is referred to the web version of this article.)

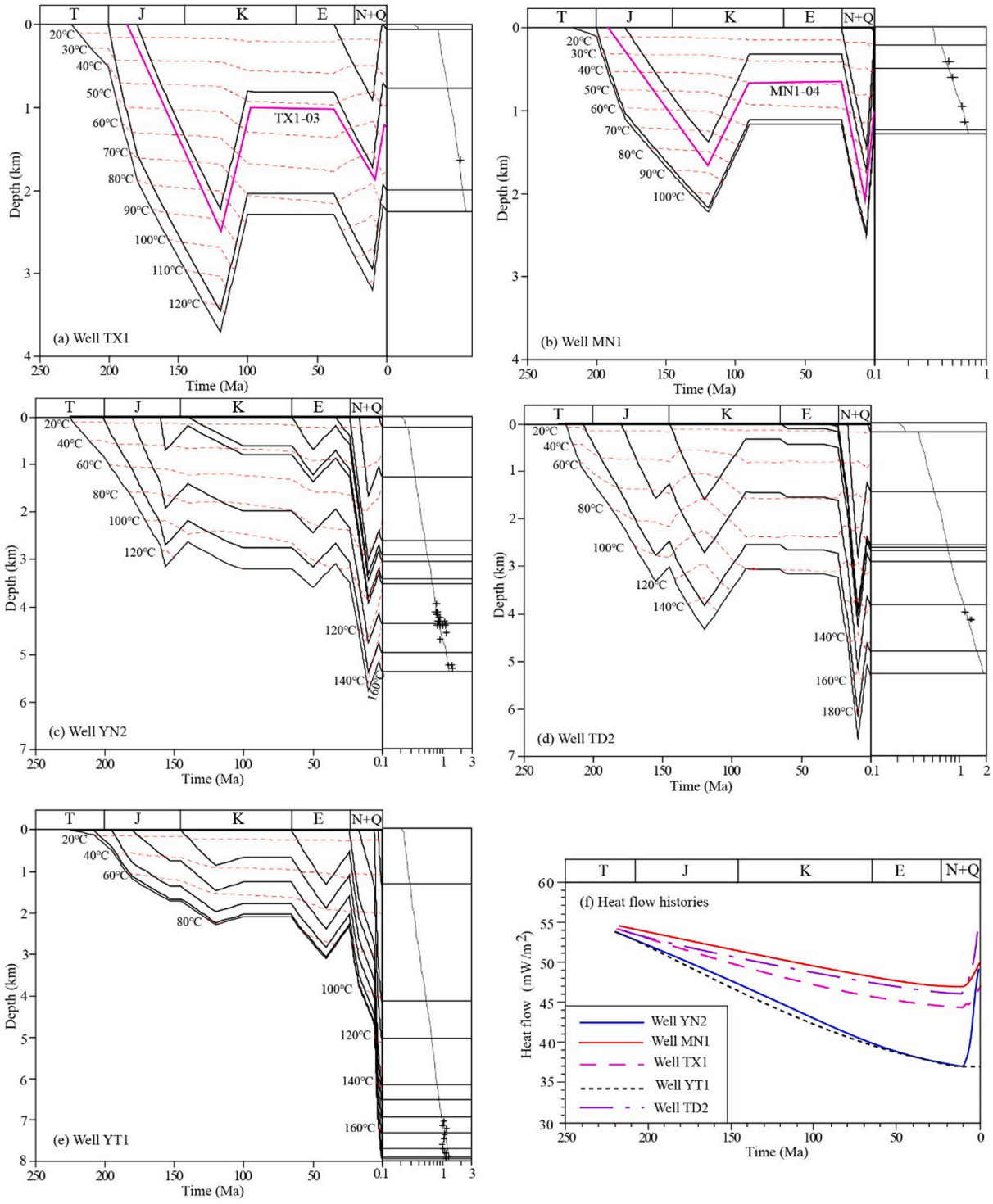

Fig. 7. (a-e) Burial and temperatrue history of the wells TX1, MN1, YN2, TD2 and YT1 (left) and the correlation of the measured Ro data (+) and simulated result with black lines (right). (f) The heat flow evolution of the typical wells in the eastern KFTB.

iteratively adjusted the paleo-heat flow paths through forward modeling and analyzed the correlation between the modeled Ro paths and the measured Ro data. The paleo-heat flow path corresponding to the actual heat flow history was considered when the modeled Ro path overlapped with the measured Ro data. Fig. 7 illustrates the burial and thermal histories of the wells TX1, MN1, YN2, TD2 and YT1, along with the reconstructed heat flow histories.

Evidently, the heat flow evolution in the eastern KFTB was influenced by regional depositional characteristics and thrust fault activities. Previous studies by Li et al. (2014) and Chang et al. (2016) suggested that rapid subsidence can lead to a thermal underbalance near the surface, resulting in a decrease in surface heat flow. Considering their similar burial histories, the heat flow evolutionary histories of wells TX1, MN1 and TD2 exhibit resemblances. During the Late Triassic, their paleo-heat flow values were around 54 ~ 55 mW/m^2. Subsequently, they gradually decreased to approximately 44–47 mW/m^2 in the Early Miocene. However, due to friction heat and local heat convection associated with Late Cenozoic thrusting (Wang et al., 2003), the heat

flow in these wells began to increase again and is currently around 47 ~ 54 mW/m^2. In contrast, well YN2 experienced relatively rapid subsidence before the Late Miocene compared to wells TX1, MN1, and TD2. Consequently, its paleo-heat flow rapidly decreased from ~ 54 mW/m^2 in the Late Triassic to ~ 37 mW/m^2 in the Early Miocene. Subsequently, along with thrust fault activity, the heat flow in well YN2 increased to approximately 54 mW/m^2 today (Figs. 1 and 7). As for the well YT1 area, it experienced a long-term rapid subsidence without substantial uplift and exhumation. Consequently, its heat flow gradually decreased from ~ 54 mW/m^2 in the Late Triassic to ~ 37 mW/m^2 today.

6. Thermal evolution of the main source rocks in the eastern KFTB

The KFTB contains several distinct suites of source rocks that formed during the Mesozoic. In this study, we focus on analyzing the maturation evolution process of the Upper Triassic Huangshanjie Formation and the Lower Jurassic Yangxia Formation source rocks in wells TD2, YN2, MN1, YT1, KZ1, TZ2 and DN201 (Fig. 8). The source rocks in wells KZ1 and MN1 areas experienced similar maturation evolution process, but the maturity levels in well KZ1 area are consistently higher than those in well MN1 area. During the Early Cretaceous, the accelerated subsidence in the well KZ1 area led to an increased maturity of the source rocks of the Huangshanjie and Yangxia formations, reaching approximately 2.4% and 1.3%, respectively. Afterward, their maturation evolution ceased since the Late Cretaceous. The maximum maturation levels of the source rocks in the well MN1 area were around 0.7% and 0.45% respectively. The continuous deposition caused that the source rocks of the well DN201 gradually increase since the deposition to be 2.4% and 1.3% by now. The Huangshanjie Formation source rock of the wells TZ2 and YN2 get into middle maturation stage with 0.7–0.9% in the Late Jurassic, followed by a long-term quiescent stage from the Late Jurassic to Early Miocene, and finally increased to be 1.3% (high maturation stage). The Huangshanjie Formation source rock of the Well YT1 experienced similar maturation evolution with the wells TZ2 and YN2, but the maturity level was always lower than them. The Huangshanjie Formation source rock of the Well TD2 get into high maturation with ~ 1.2% during the Early Cretaceous, then followed by a long-term ceasing from the Late Cretaceous to Early Miocene and finally become ~ 1.8% during the Late Miocene for wet gas generation.

The maturation evolution of the Yangxia Formation source rock in the seven wells analyzed shares similarities with the Huangshanjie Formation (Fig. 8), albeit with smaller magnitudes. Based on the maturation histories, the Huangshanjie Formation source rocks in the wells KZ1, DN201, and TD2 have reached a level of maturity where they are presently generating gas. However, the Huangshanjie Formation source rocks in the wells YN2, MN1, YT1, and TZ2, as well as the Yangxia Formation source rocks in all the wells, are still generating oil at present. These understandings can be confirmed by measured vitrinite reflectance and drilling exploration (Fig. 7; Wei et al., 2021; Wang et al., 2021).

7. Discussion

7.1. The Mesozoic-Cenozoic tectono-thermal evolution in the KFTB

The thermal modeling results in this study revealed that the eastern KFTB experienced the Cretaceous and late Miocene cooling events since the Mesozoic. The results also indicate that the cooling events occurred at different times across various areas. In the Yaha Section, the Cretaceous rapid cooling occurred in 100–60 Ma, while others areas such as wells MN1-04 and TX1-03 and Yangxia Section experienced cooing event around 120–80 Ma. This cooling event is also different from that occured in the Kalpin thrust-and-fold belt (140 ~ 120 Ma, Chang et al., 2019), Kashgar thrust-and-fold belt (100–80 Ma; Sobel et al., 2006), Bayanbulake Basin in the Central Tianshan (200–150 Ma; Jolivet et al., 2010) and Kuluktag Mountain (200 ~ 140 Ma; Zhang et al., 2011). Previous studies considered that these cooling events in Central Asia are probably realted to the collisions between the Qiangtang and Lhasa Terranes with the southern margin of the Eurasia Plate (Dumitru et al., 2001; Jolivet et al., 2010), the closure of the Mongol-Okhotsk Ocean (Jolivet et al., 2010; Wang et al., 2018) and/or the strike-slip deformation as a result of differential rotation of local curstal blocks (Yin et al., 2023). Most of Central Asia developed a paleo-planation surface and underwent gradual uplift and exhumation from the Late Jurassic to Early Cenozoic, as suggested by Morin et al. (2019) and Jolivet (2015), which could result in the differential cooling time across the Tianshan and adjacent areas. In addition, river incision played a role in localized and asynchronous erosion in the piedmonts and orogenic belts of Central Asia (Larsen and Montgomery, 2012; Malatesta and Avouac, 2018; Lu et al., 2018), probably causing variations in the timing and duration of the cooling events in the Kuqa fold-and-thrust belt and other mentioned areas. The mountain landscapes arise from interactions among tectonic rock uplift, river incision and landslide erosion (Larsen and Montgomery, 2012). Malatesta and Avouac (2018) considered that the piedmont of Eastern Tianshan were deeply incised by rivers since the Quaternary. Li et al. (2004) proposed that the elevation difference between the South Tianshan and the KFTB gradually increased since the Late Jurassic, facilitating the development of river incision. A marine transgression during the Paleogene led to renewed deposition in the Yaha Section and increased burial temperatures for samples YH-03 and YH-08, as indicated by the thermal modeling results. However, this marine transgression did not extend to the eastern part of the Yaha Section (Song et al., 2021). Therefore, samples YX-06, MN1-04 and TX-03 did not experienced the temperature increase reflected in the thermal modeling results.

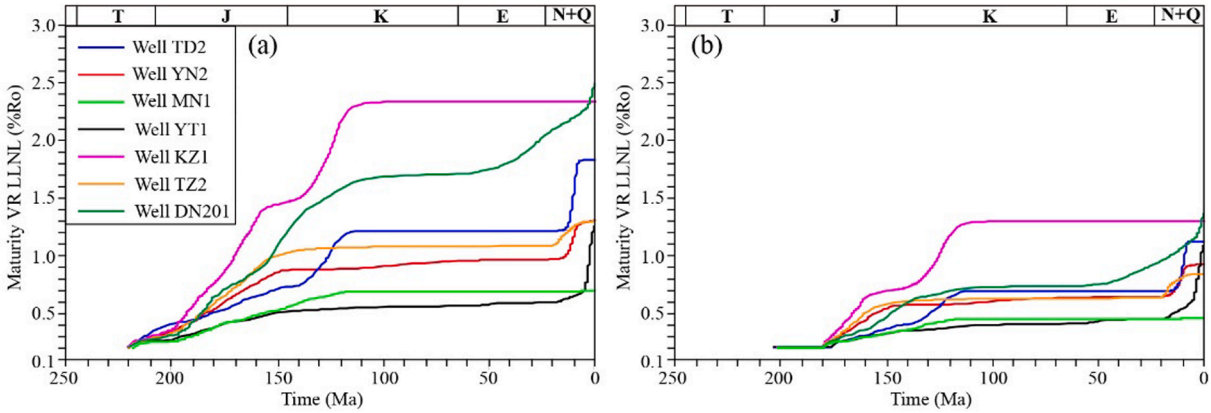

Fig. 8. The source rock maturation histories of the wells in the eastern KFTB. (a) Huanghejie Formation; (b) Yangxia Formation.

The collision between the Eurasia and India plates had a distant impact on the geological evolution of the Tianshan and adjacent basins, such as the northern margin of the Tarim Basin. Extensive research has demonstrated that compressional tectonic deformation in the KFTB commenced around 24 Ma and gradually propagated southward (Yin et al., 1998; Wang et al., 2011; Chang et al., 2017). The thermal modeling results provide valuable insights into the cooling events that occurred at different times within the eastern KFTB. The sample YH-08 indicates a cooling event around 20 Ma, while samples YX-06 and TX1-03 suggest a cooling event initiated around 10 Ma. Additionally, samples MN1-04 reveal a cooling event that began approximately 5 Ma ago. The recognition indicated that the tectonic deformation in the eastern KFTB propagated southward since the Neogene (Yu et al., 2014). According to the AFT data, Yang et al. (2017) suggested that the western KFTB experienced one cooling event during 14–11 Ma. These thermal modeling results not only highlight the variations in cooling times but also hint at the asynchronous tectonic deformation and exhumation that likely occurred in different areas or tectonic units of the KFTB during the Neogene period. The dynamic mechanism for the differential tectono-thermal evolution in the eastern and western KFTB probably include three aspects: (1) GPS data suggest the crustal shortening rate in the Tianshan decrease from west to east (Wang et al., 2001), which could result in the differential shortening and deformation in the KFTB; (2) As the detachment layers, the gypsum-salt rocks in the western KFTB dominantly experienced the plastic deformation (Tang et al., 2004, 2006; Wang et al., 2009b; Li et al., 2012; Liu et al., 2017), which should make a contribution to the differential deformation between the eastern and western KFTB. The tectonic deformation of the strata overlying the salt layers is mainly characterized by the detachment fold and thrust fault in the western KFTB (Yang, 2017). (3) the differntial uplifting in the South Tianshan during the Cenozoic provide different amounts of sediments for the eastern and western KFTB (Macaulay et al., 2013; Morin et al., 2019; Chang et al., 2021, 2022). Macaulay et al. (2013) considered that the western South Tianshan (Terskey Range) experienced rapid uplifting and exhumation since 26–20 Ma with a significant increase in exhuamtion at ~ 10 Ma. Chang et al. (2021) suggested that the Middle Tianshan experienced two phases of accelerated cooling and exhumaition at 10 ~ 6 Ma and since ~ 3 Ma. The occurrence of the plaeo-planation surface in the eastern South Tianshan implied that it only experienced slow uplifting and exhumation during the Cenozoic (Morin et al., 2019; Chang et al., 2022). The rapid uplifting and exhumation in the middle South Tianshan led the Baicheng Sag in the western KFTB to deposit massive sediments with the thickness of ~ 5–7 km, while the eastern KFTB just deposit relatively little deposits along with the slow uplifting and exhumation of the eastern South Tianshan.

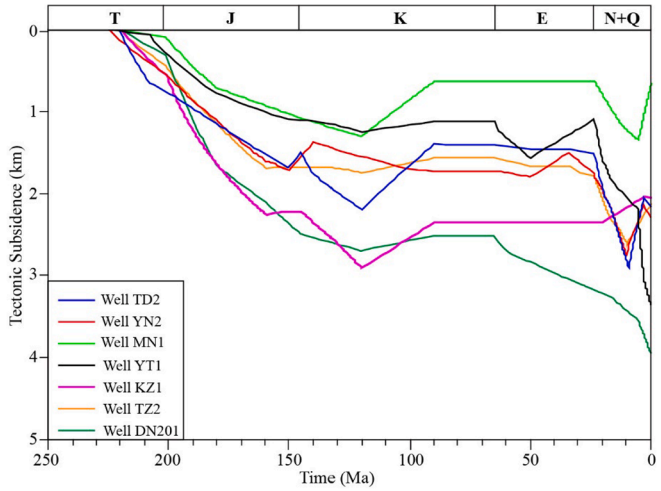

Fig. 9. The tectonic subsidence of the wells in the eastern KFTB.

The tectonic subsidence patterns in the wells TD2, YN2, MN1, YT1, KZ1, TZ2, and DN201 in the KFTB exhibit notable differences (Fig. 9), especically during the Late Cenozoic period. Moreover, the central South Tianshan experienced rapid uplifting and erosion since ~ 10 Ma, leading to significant sediment deposition in the Baicheng Sag of the western KFTB (Chang et al., 2021, 2022). In contrast, the eastern South Tianshan witnessed slower uplifting and erosion, resulting in insufficient sediment supply for the Yangxia Sag in the eastern KFTB. This differential sediment quantity has resulted in a higher maturity level for the Triassic and Jurassic source rocks in the Baicheng Sag composed to those in the Yangxia Sag (this study; Wang et al., 2021). Acccording to Wang et al. (2003), the present-day geothermal gradient in the KFTB gradually increases from south to north due to frictional heat and local heat convection along with the motion of the thrust faults. This has also led to an increase in paleo-heat flow in some wells during the Late Cenozoic. However, the heat flow in the central Tarim Basin has gradually decreased since the Late Permian (Li et al., 2022; Chang et al., 2022).

7.2. Implication for the hydrocarbon accumulation in the eastern KFTB

The oil and gas exploration results show that the eastern KFTB mainly contains the structural-lithological and tight-sandstone condensate gas reservoirs, which are distributed in the Tugeerming anticline and its adjacent areas, as well as the Dibei-Tuzi area (Wang et al., 2021, 2022; Fig. 1a). The TD2 gas reservoir in the Tugeerming anticline and its adjacent areas is classified as a normal temperature and pressure structural-lithological condensate gas reservoir with geological reserves of 200 × 10^8 m^3 (Wang et al., 2021). The reservoir strata consist of the Jurassic Kezilenur and Yangxia formations. Zhao et al. (2015) considered that the timing of crude oil and the natural gas charging was 13–8 Ma and 5–0 Ma, respectively, which were well consistent with the thermal history of the well TD2 in this study. Although oil and gas shows have been observed in the Kezilenur and Yangxia formations of the wells TX1 and MN1, they did not form reservoirs due to the Late Miocene destruction caused by intense uplifting and erosion (Wei et al., 2021; Fig. 5). The Dibei gas reservoir in the Dibei-Tuzi area is characterized by normal temperature and high-ultrahigh pressure. The reservoir stratum is the Late Jurassic Ahe Formation. The thick-layer tight sandstone of the Ahe Formation exhibits strong heterogeneity, resulting in localized accumulation of oil and gas as the lithological reservoirs (Wang et al., 2022). The homogenization temperatures of associated saline inclusions in well YN2 are gathered in 90-120℃ for crude oil charging and 140 ~ 150℃ for natural gas charging (Wang et al., 2022). According to the new burial and thermal history of the well YN2 (Fig. 7c), we considered that the charging of the crude oil and the natural gas occurred in 24 ~ 18 Ma and 5–1 Ma, respectively. These findings are consistent with the results obtained through autogenic illite K-Ar dating regarding the oil charging time (Wei, 2019). The overpressure formation and fracture development in the Late Miocene provided the driving force and pathways for oil and gas migration (Wang et al., 2023).

8. Conclusions

This study provides a detailed investigation into the tectono-thermal history of the eastern KFTB using new vitrinite reflectance, AFT and AHe data. Thermal modeling results reveal two distinct periods of rapid cooling during the Cretaceous and Miocene, which varied in timing and magnitude across different areas of the eastern KFTB. This study also clarified the heat flow historis of the eastern KFTB, which were 54 ~ 55 mW/m^2 during the Late Triassic, gradually decreased to 44 ~ 47 mW/m^2 in the Early Miocene. Subsequently, some areas in the eastern KFTB experienced an increase in paleo-heat flow during the late Miocene, likely due to thrust fault activity. Furthermore, the new maturation evolution histories revealed that the Huangshanjie Formation soure rock in the eastern KFTB have entered the gas generation stage since the late Miocene, while the Yangxia Formation source rock still retains the

potential for oil generation. Overall, this research enhances our understanding of the tectono-thermal evolution of the eastern KFTB and provides valuable information for the assessment of hydrocarbon potential in the region.

CRediT authorship contribution statement

Jian Chang: Conceptualization, Data curation, Formal analysis, Funding acquisition, Methodology, Project administration, Supervision. **Lei Yang:** . **Chenxing Li:** . **Nansheng Qiu:** . **Haizu Zhang:** . **Xiang Wang:** Data curation.

Declaration of Competing Interest

The authors declare that they have no known competing financial interests or personal relationships that could have appeared to influence the work reported in this paper.

Data availability

The data that has been used is confidential.

Acknowledgments

This work was supported by the National Natural Science Foundation of China (No. 41972125, 42272135 and U19B6003). We thank two anonymous reviewers and Editor Michel Faure for their Comments that were helpful in improving the manuscript.

References

Chang, J., Glorie, S., Qiu, N., Min, K., Xiao, Y., Xu, W., 2021. Late Miocene (10.0~6.0 Ma) rapid exhumation of the Chinese South Tianshan: Implications for the timing of aridification in the Tarim Basin. Geophys. Res. Lett. 48, e2020GL090623. doi: 10.1029/2020gl090623.

Chang, J., Qiu, N.S., Zhao, X.Z., Xu, W., Xu, Q.C., Jin, F.M., Han, C.Y., Ma, X.F., Dong, X. Y., Liang, X.J., 2016. Present-day geothermal regime of the Jizhong depression in Bohai Bay Basin, East China. Chinese J. Geophys. 59, 1003–1016. In Chinese with English abstract.

Chang, J., Tian, Y., Qiu, N., 2017. Mid-Late Miocene deformation of the northern Kuqa fold-and-thrust belt (southern Chinese Tian Shan): An apatite (U-Th-Sm)/He study. Tectonophysics 694, 101–113. https://doi.org/10.1016/j.tecto.2016.12.003.

Chang, J., Li, D., Min, K., Qiu, N., Xiao, Y., Wu, H., Liu, N., 2019. Cenozoic deformation of the Kalpin fold-and-thrust belt, southern Chinese Tian Shan: New insights from low-T thermochronology and sandbox modeling. Tectonophysics 766, 416–432. https://doi.org/10.1016/j.tecto.2019.06.018.

Chang, J., Zhang, Y., Qiu, N., Li, C., 2022. Uplift and exhumation in the Tianshan, western China: New insights from detrital zircon morphology and thermochronology. Sci. China Earth Sci. 65, 449–461. https://doi.org/10.1007/s11430-021-9872-4.

Cogné, N., Chew, D.M., Donelick, R.A., Ansberque, C., 2020. LA-ICP-MS apatite fission track dating: A practical zeta-based approach. Chem. Geol. 531, 119302 https://doi.org/10.1016/j.chemgeo.2019.119302.

Crowhurst, P.V., Green, P.F., Kamp, P.J.J., 2002. Appraisal of (U-Th)/He apatite thermochronology as a thermal history tool for hydrocarbon exploration: An example from the Taranaki Basin, New Zealand. AAPG Bull. 86 (10), 1801–1819.

Dumitru, T. A., Zhou, D., Chang, E. Z., Graham, S. A., Hendrix, M. S., Sobel, E. R., Carroll, A. R., 2001. Uplift, exhumation, and deformation in the Chinese Tian Shan. in Hendrix, M.S. and Davis, G.A., eds., Paleozoic and Mesozoic tectonic evolution of central Asia: from continental assembly to intracontinental deformation. Geol. Soc. Am. Memoir, 194, 71-99.

Farley, K.A., Wolf, R.A., Silver, L.T., 1996. The effects of long alpha-stopping distances on (U-Th)/He ages. Geochim. Cosmochim. Acta 60, 4223–4229.

Flowers, R.M., Ketcham, R.A., Shuster, D.L., Farley, K.A., 2009. Apatite (U–Th)/He thermochronometry using a radiation damage accumulation and annealing model. Geochim. Cosmochim. Acta 73, 2347–2365. https://doi.org/10.1016/j.gca.2009.01.015.

Galbraith, R.F., 1981. **On statistical models for fission track counts**. Mathematical Geology 13, 471–478.

Gleadow, A.J.W., Duddy, I.R., Lovering, J.F., 1983. Fission track analysis: a new tool for the evaluation of thermal histories and hydrocarbon potential. Aust. Petrol. Explor. Assoc. J. 23, 93–102.

He, G.Y., Lu, H.F., Yang, S.F., Li, S.X., 2004. Subsiding features of the Mesozoic and Cenozoic Kuqa Basin, Northwestern China. J. Zhejiang Univ. (Science Edition) 31, 110–113. IN Chinese with English abstract.

He, D.F., Zhou, X.Y., Yang, H.J., Lei, G.L., Ma, Y.J., 2009. Geological structure and its controls on giant oil and gas fields in Kuqa Depression, Tarim Basin: a clue from new shot seismic data. Geotecton. Metallog. 33, 19–32. In Chinese with English abstract.

Huang, B., Piper, J., Peng, S., Liu, T., Li, Z., Wang, Q., Zhu, R., 2006. Magnetostratigraphic study of the Kuche Depression, Tarim Basin, and Cenozoic uplift of the Tian Shan Range, Western China. Earth Planet. Sci. Lett. 251, 346–364. https://doi.org/10.1016/j.epsl.2006.09.020.

Huang, B., Piper, J.D.A., Qiao, Q., Wang, H., Zhang, C., 2010. Magnetostratigraphic and rock magnetic study of the Neogene upper Yaha section, Kuche Depression (Tarim Basin): Implications to formation of the Xiyu conglomerate formation, NW China. J. Geophys. Res. 115, B01101. https://doi.org/10.1029/2008jb006175.

Hubert-Ferrari, A., Suppe, J., Gonzalez-Mieres, R., Wang, X., 2007. Mechanisms of active folding of the landscape (southern Tian Shan, China). J. Geophys. Res. 112, B03S09. https://doi.org/10.1029/2006jb004362.

Jolivet, M., Dominguez, S., Charreau, J., Chen, Y., Li, Y., Wang, Q., 2010. Mesozoic and Cenozoic tectonic history of the central Chinese Tian Shan: Reactivated tectonic structures and active deformation. Tectonics 29, TC6019. https://doi.org/10.1029/2010tc002712.

Jolivet, M., 2015. Mesozoic tectonic and topographic evolution of Central Asia and Tibet: a preliminary synthesis. In: Brunet, M.F., McCann, T., Sobel, E.R. (Eds.), Geological Evolution of Central Asian Basins and the Western Tien Shan Range. Geological Society, London, Special Publications, 427, 19-55.

Ketcham, R.A., 2005. Forward and inverse modeling of low-temperature thermochronometry data. Rev. Mineral. Geochem. 58, 275–314.

Ketcham, R.A., 2016. HeFTy manual, Version 1.9.1. the University of Texas at Austin, Austin.

Ketcham, R.A., Carter, A., Donelick, R.A., Barbarand, J., Hurford, A.J., 2007. Improved measurement of fission-track annealing in apatite using c-axis projection. Am. Mineral. 92, 789–798. https://doi.org/10.2138/am.2007.2280.

Larsen, I., Montgomery, D., 2012. Landslide erosion coupled to tectonics and river incision. Nat. Geosci. 5, 468–473. https://doi.org/10.1038/ngeo1479.

Li, D., Chang, J., Qiu, N., Wang, J., Zhang, M., Wu, X., Han, J., Li, H.L., Ma, A.L., 2022. The thermal history in sedimentary basins: A case study of the central Tarim Basin, Western China. J. Asian Earth Sci. 229, 105149.

Li, W.Z., Jiao, Y.X., Zuo, Y.H., Song, X.Y., Qiu, N.S., 2014. Effect of deposition rate on geothermal field in Bozhong depression, Bohai Bay Basin. Chinese J. Geophys. 57, 1568–1577. In Chinese with English abstract.

Li, Z., Song, W., Peng, S., Wang, D., Zhang, Z., 2004. Mesozoic-Cenozoic tectonic relationships between the Kuqa subbasin and Tian Shan, northwest China: constraints from depositional records. Sed. Geol. 172, 223–249. https://doi.org/10.1016/j.sedgeo.2004.09.002.

Li, S., Wang, X., Suppe, J., 2012. Compressional salt tectonics and synkinematic strata of the western Kuqa foreland basin, southern Tian Shan, China. Basin Res. 24, 475–497. https://doi.org/10.1111/j.1365-2117.2011.00531.x.

Liu, S., Yang, X., Qiu, N., Yang, S., Li, X., 2017. Geothermal effects of salt structures on marine sedimentary basins and implications for hydrocarbon thermal evolution. Chin. Sci. Bull. 62, 1631–1644 in Chinese with English abstract.

Lu, H., Cheng, L., Wang, Z., Zhang, T., Lü, Y., Zhao, J., Li, Y., Zheng, X., 2018. Latest Quaternary rapid river incision across an inactive fold in the northern Chinese Tianshan foreland. Quat. Sci. Rev. 179, 167–181.

Lu, H.F., Jia, D., Chen, C.M., Liu, Z.H., Wang, G.Q., Jia, C.Z., 1999. Nature and timing of the Kuqa Cenozoic structures. Earth Sci. Front. 6, 215–221. In Chinese with English abstract.

Macaulay, E.A., Sobel, E.R., Mikolaichuk, A., Landgraf, A., Kohn, B., Stuart, F., 2013. Thermochronologic insight into late Cenozoic deformation in the basement-cored Terskey Range. Kyrgyz Tien Shan, Tectonics 32, 487–500. https://doi.org/10.1002/tect.20040.

Malatesta, L.C., Avouac, J., 2018. Contrasting river incision in north and south Tian Shan piedmonts due to variable glacial imprint in mountain valleys. Geology 46 (7), 659–662. https://doi.org/10.1130/G40320.1.

Mazurek, M., Hurford, A.J., Leu, W., 2006. Unravelling the multi-stage burial history of the Swiss Molasse Basin: integration of apatite fission track, vitrinite reflectance and biomarker isomerisation analysis. Basin Res. 18, 27–50.

Meesters, A.G.C.A., Dunai, T.J., 2002. Solving the production–diffusion equation for finite diffusion domains of various shapes: Part I. Implications for low-temperature (U–Th)/He thermochronology. Chemical Geology 186 (3–4), 333–344.

Morin, J., Jolivet, M., Barrier, L., Laborde, A., Li, H., Dauteuil, O., 2019. Planation surfaces of the Tian Shan Range (Central Asia): insight on several 100 million years of topographic evolution. J. Asian Earth Sci. 177, 52–65. https://doi.org/10.1016/j.jseaes.2019.03.011.

Qiu, N., Chang, J., Zhu, C., Liu, W., Zuo, Y., Xu, X., Li, D., 2022. Thermal regime of sedimentary basins in the Tarim, Upper Yangtze and North China Cratons, China. Earth-Sci. Rev. 224, 103884.

Shuster, D.L., Flowers, R.M., Farley, K.A., 2006. Theinfluence of natural radiation damage on helium diffusionkinetics in apatite. Earth Planet. Sci. Lett. 249 (3–4), 148–161.

Sobel, E., Chen, J., Heermance, R., 2006. Late Oligocene-Early Miocene initiation of shortening in the Southwestern Chinese Tian Shan: Implications for Neogene shortening rate variations. Earth Planet. Sci. Lett. 247, 70–81. https://doi.org/10.1016/j.epsl.2006.03.048.

Song, J.P., Tian, P.P., Dai, J.J., Yang, L.G., Dai, R.R., Guo, X.Y., 2021. Distribution characteristics of gypsum-salt rock and petroleum geological significance in Kuqa Depression of Tarim Basin. Fault-Block Oil & Gas Field 28, 800–804. In Chinese with English abstract.

Sweeney, J.J., Burnham, A.K., 1990. Evaluation of a simple model of vitrinite reflectance based on chemical kinetics. AAPG Bulltin 74, 1559–1570.

Tang, L.J., Jin, Z.J., Jia, C.Z., Pi, X.J., Chen, S.P., Xie, H.W., Wang, Z.Y., 2004. A large-scale salt nappe complex in the leading edge of the Kuqa foreland fold-thrust belt, Tarim Basin, Northwest China. Acta Geol. Sin. 78, 17–25. In Chinese with English abstract.

Tang, L.J., Li, J.C., Yu, Y.X., Wang, Q.H., Yang, W.J., Xie, H.W., Chen, S.P., Peng, G.X., 2006. Differential salt tectonic deformation and segmentation of the Kuqa foreland fold-thrust belt, Tarim Basin, Northwest China. Acta Geol. Sin. 80, 313–320. In Chinese with English abstract.

Tang, X.Y., Yang, S.C., Hu, S.B., 2014. Thermal and maturation history of Jurassic source rocks in the Kuqa foreland depression of Tarim Basin, NW China. J. Asian Earth Sci. 89, 1–9.

Vermeesch, P., 2010. HelioPlot, and the treatment of overdispersed (U-Th-Sm)/He data. Chem. Geol. 271, 108–111.

Vermeesch, P., 2018. IsoplotR: a free and open toobox for geochronology. Geosci. Front. 9, 1479–1493.

Wang, Y.N., Cai, K.D., Sun, M., Xiao, W.J., De Grave, J., Wan, B., Bao, Z.H., 2018. Tracking the multi-stage exhumation history of the western Chinese Tianshan by apatite fission track (AFT) dating: implications for the preservation of epithermal deposits in the ancient orogenic belt. Ore Geol. Rev. 100, 111–132.

Wang, Q., Zhang, P., Freymueller, J.T., Bilham, R., Larson, K.M., Lai, X., You, X., Niu, Z., Wu, J., Li, Y., Liu, J., Yang, Z., Chen, Q., 2001. Present-day crustal deformation in China constrained by global positioning system measurements. 294, 574-577.

Wang, X., Suppe, J., Guan, S.W., Hubert-Ferrari, A., Gonzalez-Mieres R., Jia, C.Z., 2011. Cenozoic Structure and Tectonic Evolution of the Kuqa Fold Belt, Southern Tianshan, China. In McClay K., Shaw, J.H., and Suppe, J., eds., Thrust fault-related folding. AAPG Memoir, 94, 215-243. doi:10.1306/13251339m94389.

Wang, L.S., Li, C., Liu, S.W., Li, H., Xu, M.J., Wang, Q., Ge, R., Jia, C.Z., Wei, G.Q., 2003. Geotemperature gradient distribution of Kuqa Foreland Basin, north of Tarim, China. Chin. J. Geophys. 46, 403–407. In Chinese with English abstract.

Wang, Q., Li, S., Du, Z., 2009a. Differential uplift of the Chinese Tianshan since the Cretaceous: constraints from sedimentary petrography and apatite fission-track dating. Int. J. Earth Sci. 98, 1341–1363. https://doi.org/10.1007/s00531-009-0436-2.

Wang, B., Qiu, N.S., Littke, R., Amberg, S., Liu, Z.D., 2023. Petroleum system modelling in a compressional tectonic setting: the eastern Kuqa Depression, Tarim Basin, Northwestern China. J. Asian Earth Sci. 249, 105612.

Wang, X., Tang, P.C., Xie, H.W., Lei, G.L., Huang, S.Y., 2009b. Cenozoic salt structure and evolution in the western Kuqa Depression, Tarim Basin, China. Geotecton. Metallog. 33, 57–65. In Chinese with English abstract.

Wang, K., Yang, H.J., Li, Y., Zhang, R.H., Ma, Y.J., Wang, B., Yu, C.F., Yang, Z., Tang, Y. G., 2021. Geological characteristics and exploration potential of the northern tectonic belt of Kuqa depression in Tarim Basin. Acta Pet. Sin. 42, 885–905. In Chinese with English abstract.

Wang, Q.H., Zhang, R.H., Yang, X.Z., Yu, C.F., Xu, Z.P., Zhou, L., Wang, K., Zhang, L., 2022. Major breakthough and geological significance of tight sandstone gas exploration in Jurassic Ahe Formation in Dibei area, eastern Kuqa depression. Acta Pet. Sin. 43, 1049–1064. In Chinese with English abstract.

Wei, Q., 2019. Research on accumulation characteristics and model of deep-buried tight sandstone gas in the Kuqa Depresssion. China University of Mining & Technology-Beijing. PhD thesis.

Wei, H.X., Huang, W.H., Luo, H.N., Li, L., Shi, L.L., Wang, Z.T., 2016. Faults characteristics and evolution in the eastern Kuqa Depression. Earth Sci. 41, 1074–1080. In Chinese with English abstract.

Wei, G.Q., Zhang, R.H., Zhi, F.Q., Wang, K., Yu, C.F., Dong, C.Y., 2021. Formation conditions and exploration directions of Mesozoic structural-lithologic stratigraphic reservoirs in the eastern Kuqa depression. Acta Pet. Sin. 42, 1113–1125. In Chinese with English abstract.

Wu, L., Monié, P., Wang, F., Lin, W., Ji, W.B., Bonno, M., Münch, P., Wang, Q.C., 2016. Cenozoic exhumation history of Sulu terrane: Implications from (U–Th)/He thermochrology. Tectonophysics 672–673.

Xu, W., Wang, W., Yin, H., Jia, D., Yang, G., Li, G., 2020. Numerical simulation of different subsalt structural features and their evolution in the eastern and western segments of the Kuqa depression. Acta Geol. Sin. 94 (6), 1740–1751 in Chinese with English abstract.

Yang, W., Li, J., Guo, Z., Jolivet, M., Heilbronn, G., 2017. New apatite fission-track ages of the western Kuqa Depression: implications for the Mesozoic-Cenozoic tectonic evolution of South Tianshan, Xinjiang. Acta Geol. Sinica (English Edition) 91 (2), 396–413.

Yang, K.J., 2017. Differential structural deformations and controlling factors of salt tectonic in the middle segment of the Kuqa Depression. Ph.D. Dissertation. Beijing: China University of Petroleum, Beijing, 1-123. (In Chinese with English abstract).

Yin, A., Nie, S., Craig, P., Harrison, T.M., Ryerson, F.J., Xianglin, Q., Geng, Y., 1998. Late Cenozoic tectonic evolution of the southern Chinese Tian Shan. Tectonics 17, 1–27. https://doi.org/10.1029/97tc03140.

Yin, J., Wang, Y., Hodges, K.V., Xiao, W., Thomson, S.N., Chen, W., Yuan, C., Sun, M., Cai, K., Sun, J., 2023. Episodic long-term exhumation of the Tianshan Orogenic belt: new insights from multiple low-temperature thermochronometers. Tectonics 42.

Yu, S., Chen, W., Lü, X., Evans, N., McInnes, B., Yin, J., Sun, J., Li, J., 2014. (U-Th)/He thermochronometry constraints on the Mesozoic-Cenozoic tectono-thermal evolution of Kuqa basin: a case study of well TZ2. Chinese J. Geophys. 57, 62–74. In Chinese with English abstract.

Zhang, T., Fang, X.M., Song, C.H., Appel, E., Wang, Y.D., 2014. Cenozoic tectonic deformation and uplift of the South Tian Shan: Implications from magnetostratigraphy and balanced cross-section restoration of the Kuqa depression. Tectonophysics 628, 172–187. https://doi.org/10.1016/j.tecto.2014.04.044.

Zhang, Z., Zhu, W., Shu, L., Wan, J., Yang, W., Zheng, B., Su, J., 2011. Multi-stage exhumation of the NE Tarim Precambrian bedrock, NW China: constraints from apatite fission track thermochronology in the Kuluketage area. Terra Nova 23, 324–332. https://doi.org/10.1111/j.1365-3121.2011.01017.x.

Zhang, Z., Shen, Z., Sun, J., Wang, X., Tian, Z., Pan, X., Shi, L., 2015. Magnetostratigraphy of the Kelasu section in the Baicheng depression, Southern Tian Shan, northwestern China. J. Asian Earth Sci. 111, 492–504. https://doi.org/10.1016/j.jseaes.2015.06.016.

Zhang, Z., Sun, J., Tian, Z., Gong, Z., 2016. Magnetostratigraphy of syntectonic growth strata and implications for the late Cenozoic deformation in the Baicheng Depression, Southern Tian Shan. J. Asian Earth Sci. 118, 111–124. https://doi.org/10.1016/j.jseaes.2015.12.024.

Zhang, Z., Sun, J., Tian, S., Lü, L., Su, B., Cao, M., Li, J., Li, Y., 2020. Environmental magnetic evidence for enhanced aridification in the Tarim Basin since ~5.3 Ma, NW China. J. Asian Earth Sci. 189, 104181 https://doi.org/10.1016/j.jseaes.2019.104181.

Zhao, M.J., Lu, X.S., Zhuo, Q.G., Li, Y., Sang, Y., Lei, G.L., Wang, Y., 2015. Characteristics and distribution law of hydrocarbon accumulation in Kuqa foreland basin. Acta Pet. Sin. 36, 395–404. In Chinese with English abstract.